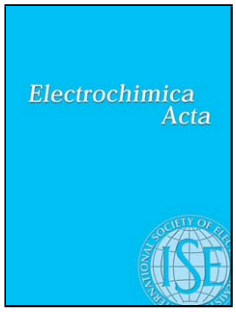

Title: Electrocatalytic activity of IrO_2–RuO_2 supported on Sb-doped SnO_2 nanoparticles

Authors: Aaron T. Marshall, Richard G. Haverkamp

PII: S0013-4686(09)01379-6
DOI: doi:10.1016/j.electacta.2009.11.018
Reference: EA 15171

To appear in: *Electrochimica Acta*

Received date: 6-5-2009
Revised date: 6-11-2009
Accepted date: 6-11-2009

Please cite this article as: A.T. Marshall, R.G. Haverkamp, Electrocatalytic activity of IrO_2–RuO_2 supported on Sb-doped SnO_2 nanoparticles, *Electrochimica Acta* (2008), doi:10.1016/j.electacta.2009.11.018

Electrocatalytic activity of IrO_2–RuO_2 supported on Sb-doped SnO_2 nanoparticles

Aaron T. Marshall[a], Richard G. Haverkamp[b]

[a] *Department of Chemical and Process Engineering, University of Canterbury, Christchurch, New Zealand*
[b] *School of Engineering and Advanced Technology, Massey University, Palmerston North, New Zealand*

Abstract

Electrocatalytic IrO_2–RuO_2 supported on Sb-doped SnO_2 (ATO) nanoparticles is very active towards the oxygen evolution reaction. The IrO_2–RuO_2 material is XRD amorphous and exists as clusters on the surface of the ATO. Systematic changes to the surface chemical composition of the ATO as a function of the IrO_2:RuO_2 ratio suggests an interaction between the IrO_2–RuO_2 and ATO. Cyclic voltammetry indicates that the electrochemically active surface area of IrO_2–RuO_2 clusters is maximised when the composition is 75 mol% IrO_2 - 25 mol% RuO_2. Decreasing the loading of IrO_2–RuO_2 on ATO reduces the electrochemically active surface area, although there is evidence to support a decrease in the clusters size with decreased loading. Tafel slope analysis shows that if the clusters are too small, the kinetics of the oxygen evolution reaction are reduced. Overall, clusters of IrO_2–RuO_2 on ATO have similar or better performance for the oxygen evolution reaction than many previously reported materials, despite the low quantity of noble metals used in the electrocatalysts. This suggests that these oxides may be of economic

Email address: aaron.marshall@canterbury.ac.nz (Aaron T. Marshall)

Preprint submitted to Electrochimica Acta *November 6, 2009*

advantage if used as PEM water electrolysis anodes.

Key words: Electrocatalysis, Oxygen evolution reaction, IrO_2, RuO_2, Sb doped SnO_2

1. Introduction

Hydrogen can be produced using PEM water electrolysis. In this process, water is split to give oxygen, electrons and protons at the anode. These protons are reduced at the cathode to hydrogen gas after travelling through the membrane. It is widely accepted that the anodic reaction requires the largest overpotential and thus the anode electrocatalyst has been the focus of much work [1–7]. Typically the anode electrocatalysts for acidic conditions are IrO_2 and RuO_2 based materials.

An ongoing aim of electrocatalyst research is to increase the catalyst performance while reducing the cost. As electrocatalysis involves the interaction of the electrode surface with the reactants and products, simply increasing the active surface area will increase the apparent reaction rate. One method of achieving this is to support electrocatalytic nanoparticles on high surface area materials such as carbon black. As electrocatalysts are often expensive (e.g. Pt, IrO_2), by increasing the specific surface area of the active electrocatalyst, less material is required to maintain high reaction rates, thus decreasing the cost of the electrodes. Some supports also increase the lifetime of the electrocatalyst by reducing the sintering effect [8]. Supported electrocatalysis may also benefit from enhanced specific activity related to support–electrocatalyst interactions [9–11].

One electrocatalyst support that has proved successful in PEM fuel cells

is carbon. However, carbon can be electrochemically oxidised at potentials above 0.206 V vs SHE [12], with this suggested to cause Pt nanoparticle agglomeration in carbon supported Pt [13]. Prolonged oxidation is also suggested to decrease the electrical conductivity of the catalytic layer as well as cause a loss in the layers mechanical integrity [14]. As PEM water electrolysis anodes operate at high anodic potentials (> 1.5V vs SHE), the long-term use of carbon in the PEM water electrolysis anode environment is not possible. Thus an alternative support material must be found if the advantages obtained by supporting electrocatalytic nanoparticles are to be realised in PEM water electrolysers.

Many alternatives to carbon black for electrocatalytic supports have been investigated including Sb-doped SnO_2 [8, 11], $Ru_xTi_{1-x}O_2$ [15], boron-doped diamond [14, 16, 17], Magneli phase TiO_x [18], and TiC [19]. Here we investigate Sb-doped SnO_2 as a support material due to its electrical conductivity and stability in acidic conditions [8]. Furthermore, it has been shown that SnO_2 improves the stability of IrO_2-RuO_2 anodes during oxygen evolution, even though XRD revealed little mixing of the SnO_2 with the IrO_2-RuO_2 [1]. This finding suggests that similar improvements in stability might be expected for Sb-doped SnO_2 supported $Ir_xRu_{1-x}O_2$.

2. Experimental

2.1. Oxide preparation

Metal chlorides ($IrCl_3.xH_2O$, American Elements - 99.9 % and $RuCl_3.xH_2O$, Alfa Aesar - 99.9 %) were added to dry Sb-doped SnO_2 (ATO) nanoparticles (Aldrich 99.5 %, 10 mol%Sb_2O_5) to achieve a total noble metal loading on

the ATO of 5, 10, and 20 wt%. The composition of the noble metal oxide coating was adjusted by changing the ratio of noble metal precursors added to the ATO. Deionised water (0.5 ml) was added to each sample (0.4 g) and a homogeneous suspension of ATO in the noble metal chloride solution was obtained by ultrasonic treatment for 30 minutes. This suspension was then freeze dried at -80 °C and $\leq$1 mbar overnight. This resulting dry powder was finely ground then re-suspended in 0.5 ml deionised water before being freeze dried again to ensure the dry powder was as homogeneous as possible. The dry powder (at this stage ATO coated with $IrCl_3.xH_2O$ and $RuCl_3.xH_2O$) was thermally treated in air at 450°C for 1 hour to decompose and oxidise the noble metal chlorides. This step is similar to the standard thermal decomposition method employed in the dimensionally stable anode (DSA) industry [20].

2.2. Characterisation

X-ray diffraction (XRD) was performed on the dry electrocatalytic powders at the powder diffraction beamline of the Australian Synchrotron. The X-ray beam was monochromated to 12.395 keV (λ = 0.1000 nm) and the diffraction data recorded using a MYTHEN (microstrip) detector over a 2θ range of 5 to 80 degrees with an acquisition time of 300s. The powders were held in glass capillaries (300 μm OD, 10 μm wall thickness). LaB_6 was used as a diffraction standard. The diffraction patterns were background corrected using the diffraction pattern of an empty capillary and the FWHM measured for crystal size analysis using the Scherrer Equation.

X-ray photoelectron spectroscopy (XPS) was performed on the electrocatalysts by pressing a thin layer of the dry powder into a adhesive carbon

disc. An AXIS Ultra DLD instrument was used with a monochromatic Al Kα x-ray source, with the full spectrum collected with a band pass of 160 eV and the specific regions collected with a band pass of 20 eV. An electron flood gun was used to minimise the possibility of differential charging between the ATO and noble metal oxide phases. The surface ratio of iridium, ruthenium, antimony and tin was determined by comparison of the Ir $4f_{7/2}$ Ru $3d_{5/2}$, Sb $3d_{5/2}$ and Sn $3d_{5/2}$ photoelectron lines and the use of appropriate sensitivity factors [21]. Curve fitting was carried out using Gaussian-Lorentzian type profiles (XPSPeak 4.1). Due to the overlap of the O 1s and Sb $3d_{5/2}$ lines, the area of the Sb $3d_{5/2}$ line was calculated using the 2 : 3 ratio of Sb $3d_{3/2}$: Sb $3d_{5/2}$ lines. The Sn $3d_{5/2}$ line at 487.06 eV was choosen as the reference energy as the C 1s peak around 285 eV overlaps with the Ru $3d_{3/2}$ peak.

TEM analysis was performed using a Philips CM10 instrument operating at 60 keV, by drying a small drop of the electrocatalytic particles suspended in isopropanol, onto a Formvar coated Cu grid.

Cyclic voltammetry (CV) of the oxide particles was performed in 0.5 mol L^{-1} H_2SO_4 using a Gamry G300 potentiostat. As the current response of $Ir_xRu_{1-x}O_2$ is largely psuedo–capacitive in nature, a low–pass current filter (5 Hz) was used to compensate for that fact that the potentiostat applies the potential sweep as a staircase waveform rather than a linear waveform when performing CV using a digital instrument [22]. The step size of the staircase waveform was also minimized to ensure the measured current response was close to that produced by a true linear waveform. The working electrodes were prepared by spraying an ink containing the oxide particles and Nafion ionomer (Ion Power Inc.) onto clean titanium discs held at 80 °C. Prior to

application of the oxide layer, the titanium substrates were roughened with 600 grit SiC paper, rinsed with acetone in an ultrasonic bath, followed by drying at 105 °C. The oxide layer consisted of 95 wt% electrocatalyst particles and 5 wt% Nafion and had an oxide loading of 0.8 mg cm^{-2} (determined gravimetrically within ± 0.01 mg cm^{-2}). A three electrode Teflon cell was used along with a Pt foil counter and Ag/AgCl, $NaCl_{3M}$ reference electrode, with a working electrode area of 0.385 cm^2. All potentials reported here are relative to the Ag/AgCl,$NaCl_{3M}$ reference electrode (0.209 V vs SHE). The solution was bubbled with N_2 for 30 minutes prior to the experiments and passed over the solution during the measurements. To obtain a reproducible voltammetric response, the oxide electrodes were initially subjected to 50 cycles between 0.2 and 1.2 V at 50 mV s^{-1}.

3. Results and Discussion

3.1. Particle Structure and Size

High resolution x-ray diffraction was used to identify the crystalline phases of the $Ir_xRu_{1-x}O_2$ on ATO samples. All recorded diffraction patterns exhibited a single rutile phase with lattice spacings similar to pure SnO_2 with no evidence of any IrO_2 or RuO_2 crystalline phases (Fig. 1). The crystallite size of the crystalline phase was estimated to be 29 nm based on the Scherrer Equation. As DSA type layers annealed at 450°C normally exhibit clear diffraction patterns of rutile IrO_2 or RuO_2 [20], the lack of any diffraction peaks indicates that the $Ir_xRu_{1-x}O_2$ phase must be amorphous or consist of very small crystals (< 0.5 nm). Based on an even coating of the ATO particles, the shell thickness for a loading of 20 wt% $Ir_xRu_{1-x}O_2$ on ATO

would be approximately 1 nm. This coating thickness is unlikely to support the formation of a phase with sufficient long-range ordering to be detected by XRD. The lack of $Ir_xRu_{1-x}O_2$ crystallites suggests our preparation procedure results in very high dispersion of $Ir_xRu_{1-x}O_2$ on the surface of the ATO nanoparticles.

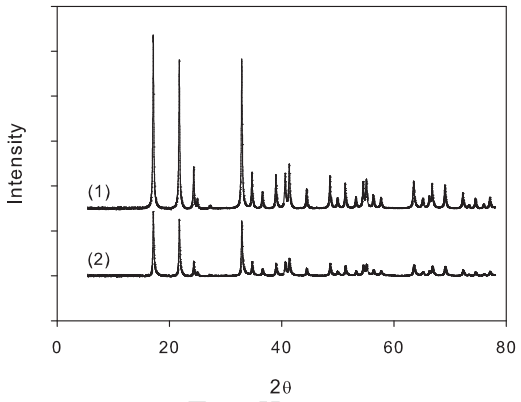

Figure 1: Powder XRD patterns of 20 wt% $Ir_xRu_{1-x}O_2$ on ATO ($\lambda = 0.1$nm). (1) ATO nanoparticles (2) $Ir_{0.5}Ru_{0.5}O_2$ on ATO.

TEM was used to characterise the particle size of the prepared electrocatalysts. The ATO nanoparticles are approximately spherical and exhibit particle sizes ranging from around 10 to 50 nm in diameter. The average particle size was estimated to be 20 nm ± 7 nm (1 Standard deviation, n=57). The difference in particle size and the crystallite size calculated from the XRD is probably related to the difference between the number size average (TEM) and the volume size average (XRD) and suggests that the ATO particles are single crystals. From this TEM work no major differences between the ATO particles and the $Ir_xRu_{1-x}O_2$ - ATO nanoparticles could be deter-

mined giving further evidence that the $Ir_xRu_{1-x}O_2$ must be either a very thin coating or consist of small clusters on the surface of the ATO.

3.2. Surface properties

As XRD measurements did not identify any crystalline phases of IrO_2 or RuO_2, x-ray photoelectron spectroscopy (XPS) was used to determine the chemical state of the Ir and Ru on the surface of the ATO. As this coating is thin, the XPS spectra will reflect the average state of the Ir and Ru materials. A XPS survey spectrum revealed the presence of Ir, Sn, Sb, O and Ru at the surface. Cl 2p photoelectron lines originating from the Ru and Ir precursors were also observed around 200 eV. We found that the binding energy of the Ru $3d_{5/2}$ line was located at 280.90 $\pm$ 0.08 eV (1 Standard deviation), corresponding to Ru^{4+}, although as the Ru 3d region is overlapped by the C 1s lines further analysis was not attempted. Analysis of the Sn 3d photoelectron lines showed that the Sn $3d_{5/2}$ binding energy (487.06 eV $\pm$ 0.03 eV) remains constant over the range of coating compositions and is consistent with Sn^{4+} in SnO_2 as is the spin-orbit splitting of 8.4 eV [24]. As expected the doping by Sb causes asymmetry in the Sn 3d lines due to screening effects [25]. The surface concentration of Ru and Ir was calculated to be around 30 mol% for the samples with a coating of 20 wt% $Ir_xRu_{1-x}O_2$. As the attenuation length of the Sb and Sn photoelectrons is close to 1 nm we can confidently rule out the possibility of an uniform and continuous coating of $Ir_xRu_{1-x}O_2$ on ATO (which we calculate would be on the order of 1 nm) due to the relatively high Sn and Sb concentrations. This indicates that samples consist of small $Ir_xRu_{1-x}O_2$ clusters supported on ATO nanoparticles.

3.2.1. Chemical state of the Iridium species

The Ir 4f region exhibits two peaks around 62.25 and 65.2 eV which correspond to the Ir $4f_{7/2}$ and Ir $4f_{5/2}$ lines respectively (Fig. 2). The Ir $4f_{7/2}$ binding energy is significantly higher than for metallic Ir (BE=60.9 eV [24]) indicating that the Ir oxidation state is consistent with a IrO_2 phase. As in most investigations, the Ir 4f region is asymmetric [26–29], with this asymmetry being successfully reproduced using a perturbation-theory treatment of the many-body screening response of the 5d electrons in rutile IrO_2 [29]. There is disagreement in literature regarding the cause of the asymmetric Ir 4f line shape in IrO_2 with some relating this to multiple oxidation states of the iridium [26, 27]. Despite the large amount of literature discussing an Ir(III) oxide phase (e.g. Ir_2O_3) we have found no literature providing structural evidence of any Ir(III) oxide phase which is stable under normal conditions. Furthermore, the asymmetry of the Ir 4f region is observed for nearly all IrO_2 samples independent of the preparation procedure and thermal history, most likely ruling out the asymmetry explanation based on multiple oxidation states [29].

By fitting the Ir 4f region to a single set of asymmetric peaks (Fig. 2) we have found that there is a small shift in the peak positions to lower binding energies as the ruthenium content in the coating increased (Ir $4f_{7/2}$ 62.2 to 61.8eV). Similar behaviour was found for samples with 5 and 10 wt% $Ir_xRu_{1-x}O_2$ coatings. While this shift is systematic with composition, we cannot rule out changes to the binding energy due to differential charging or changes in the iridium species due to the UHV conditions. The asymmetry factors required in the fitting procedure also vary systematically with

the ruthenium content (higher asymmetry as Ru content increases), which suggests that the screening response of the Ir 5d electrons is a function of the ruthenium content. It has been shown that the asymmetry of the Ir 4f lines of Ir-Ta oxides decreases as the Ta content increases, with this result suggested to be due to a reduced amount of electrons in the conduction band of Ta rich Ir-Ta oxide [28]. Here a similar argument can be used as the small IrO_2 clusters may not exhibit metallic conduction, i.e. the small clusters have similar electronic properties to amorphous IrO_2 [5, 30]. Electrochemically formed IrO_2 layers also show increased asymmetry with increased film growth, which corresponds with the appearance of the O 1s line from lattice oxide ions in crystalline IrO_2 [27]. This is consistent with the suggestion that the asymmetry of the Ir 4f region occurs due to conduction band screening in rutile structured IrO_2. We therefore suggest that the addition of Ru increases the number of electrons in the conduction band (or allows the formation of the conduction band) in the $Ir_xRu_{1-x}O_2$ due to an increase in structural order or electronic interaction between the Ir and the ATO support.

3.2.2. Chemical state of the surface Antimony species

Due to the overlap of the O 1s and Sb $3d_{5/2}$ lines (Fig. 3), analysis of the surface Sb was restricted to the Sb $3d_{3/2}$ line. This peak was fitted to a combination of two symmetrical lines with a fixed binding energies corresponding to Sb^{3+} and Sb^{5+} (BE=539.4 eV and BE=540.2 eV respectively [31]). This fit found that Sb^{5+} dominated, with the level of Sb^{3+} increasing as the Ru content of the coating increased (Fig. 3B). The reduction of Sb^{5+} can be explained by a solid–state reaction between $RuCl_3$ or $IrCl_3$ and Sb_2O_5 (Eqn 1). Based on thermochemical data [32], the reduction of Sb^{5+} will occur more

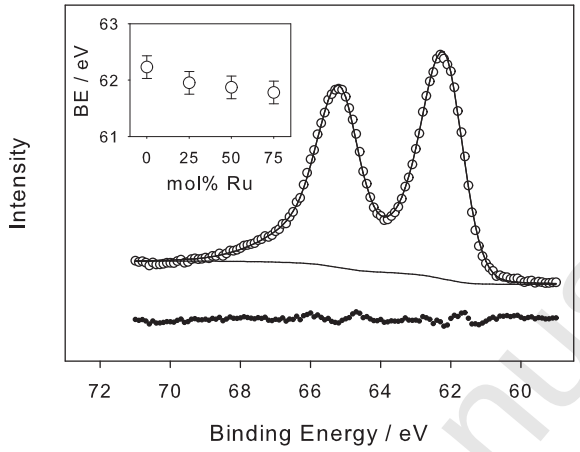

Figure 2: Typical Ir 4f region of $Ir_xRu_{1-x}O_2$ on ATO nanoparticles. ∘ - experimental data, lines - fitted peaks, • - difference curve. Insert: Ir $4f_{7/2}$ binding energy as a function of Ru content in the coating.

readily in the presence of $RuCl_3$ ($\Delta G_{reaction(700K)}$ = -1 kJ mol^{-1}) compared to $IrCl_3$ ($\Delta G_{reaction(700K)}$ = +65 kJ mol^{-1}) which is consistent with the XPS analysis.

$$Sb_2O_5 + RuCl_3 \rightleftharpoons Sb_2O_3 + RuO_2 + 1/2Cl_2 \quad (1)$$

The fact that the Sb oxidation state varies as a function of coating composition gives further evidence to support the formation of $Ir_xRu_{1-x}O_2$ on the surface of the ATO particles rather than the formation of $Ir_xRu_{1-x}O_2$ particles independent of the ATO particles. This change in oxidation state may also explain the observed Ir 4f binding energy shift. We expect a stronger electron withdrawing effect from Ir if this is supported on Sb_2O_5 rather than Sb_2O_3. Thus when the Sb species at the ATO surface are Sb_2O_5, the Ir BE

energy should be higher than if the ATO surface is predominately Sb_2O_3. Our experimental data is consistent with this, although the shift in Ir 4f binding energy may be within the level of experimental uncertainty. At low Ru contents, the support Sb species are in the Sb^{5+} state and the Ir 4f binding energy is increased due to an electron withdrawing effect. As the Ru content increases, this withdrawing effect is reduced due to the reduction in the Sb oxidation state. This hypothesis is further supported by the changes to the asymmetry of the Ir 4f photoelectron lines. With an increase in the electron withdrawing effect, the conduction band screening effect is reduced and the Ir 4f photoelectron line becomes less asymmetric. The implications of this observation are still to be resolved. In particular we are interested to see the proposed changes in the Ir and Sb properties induced by the coating composition are maintained in electrolytes rather than UHV conditions.

3.3. Electrochemical behaviour in 0.5 mol L^{-1} H_2SO_4

Cyclic voltammetry was used to characterise the electrochemical behaviour of the $Ir_xRu_{1-x}O_2$ on ATO nanoparticles. Overall the shape of the voltammograms exhibit the broad waves consistent with the shape of voltammograms measured for IrO_2, $Ir_xRu_{1-x}O_2$ and RuO_2 DSA electrodes [33, 34] (Fig. 4 A-C). The broad wave features on these oxides result from the solid–state redox reactions in which the surface Ir or Ru can be oxidised or reduced accompanied by proton exchange between the oxide and the electrolyte [35]. Thus the capacitance of the $Ir_xRu_{1-x}O_2$ on ATO nanoparticles is a combination of the pseudo–capacitance resulting from charge storage by the solid–state redox reactions and the standard double layer capacitance resulting from charge storage within the electrode–electrolyte interface. Voltammetry of the ATO

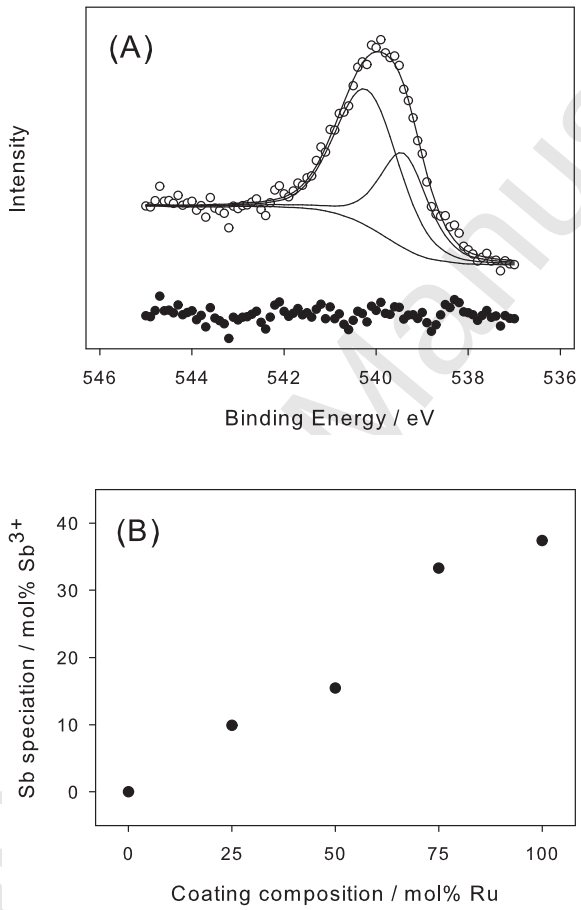

Figure 3: (A) Fitted Sb $3d_{3/2}$ region for RuO_2 on ATO nanoparticles, ∘ - experimental data, lines - fitted peaks, • - difference curve. (B) mol% Sb^{3+} vs mol% Ru in coating

nanoparticles without a noble metal oxide coating revealed that the support material had a capacitance of 20 F g^{-1} (total anodic charge extrapolated to at an infinitely slow sweep rate) equating to around 33 m^2 g^{-1} assuming a ideal capacitance of 60 μF cm^{-2} [36]. This value is of similar size to that estimated by the TEM (44 m^2 g^{-1}) and XRD (30 m^2 g^{-1}) analysis and suggests that most of the particles in the prepared electrodes contribute to the electrochemical response.

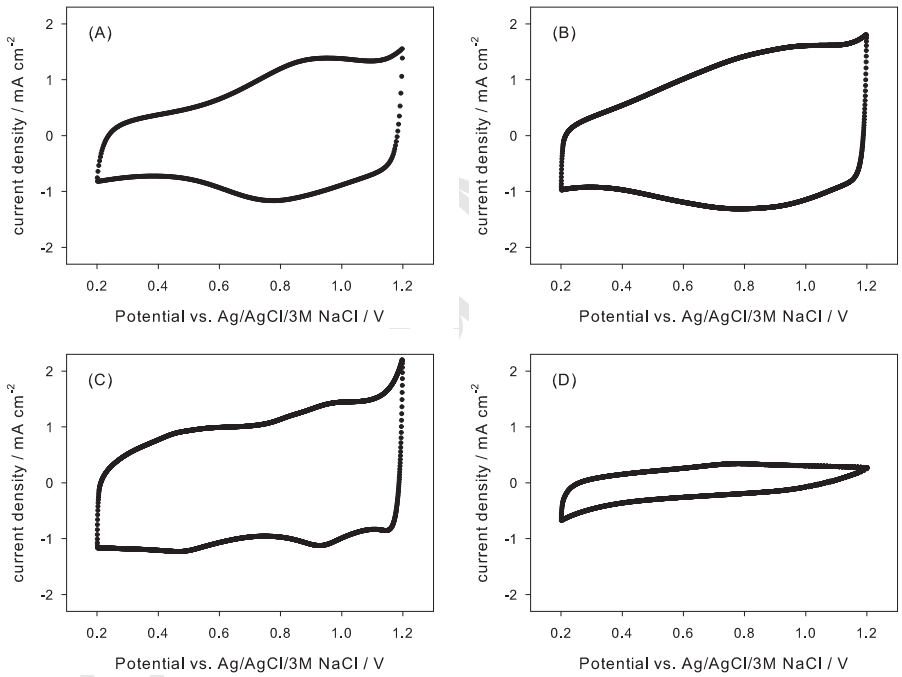

Figure 4: Cyclic voltammograms of (A) 20 wt% IrO_2 on ATO nanoparticles, (B) 20 wt% $Ir_{0.5}Ru_{0.5}O_2$ on ATO nanoparticles, (C) 20 wt% RuO_2 on ATO nanoparticles and (D) ATO nanoparticles at 20 mV s^{-1} in 0.5 mol L^{-1} H_2SO_4.

Charge measurements (integration of the anodic sweep of the voltammogram) are often used in DSA literature to compare the electrochemically

active surface area of noble metal oxide electrodes [37, 38]. Typically the charge of $Ir_xRu_{1-x}O_2$ electrodes show a strong dependence on composition [34, 39, 41]. Here we have used the approach described by others to evaluate the outer and total charge of the materials [40]. Briefly, the outer charge which represents the Ir and Ru sites which are easily accessible, is evalulated by extrapolating the charge to infinite sweep rate, whereas the total charge, which includes all electroactive Ir and Ru sites, is found by extrapolation to zero sweep rate. The outer charge varies with the $Ir_xRu_{1-x}O_2$ composition and is at a maximum around 25 mol% iridium (Fig. 5). A result of the high $Ir_xRu_{1-x}O_2$ dispersion is that the variation in charge with composition is much less than observed at DSA type layers [34, 39, 41]. This indicates that a wider composition range can be used without significant loss of electrochemically active surface area if $Ir_xRu_{1-x}O_2$ is well dispersed.

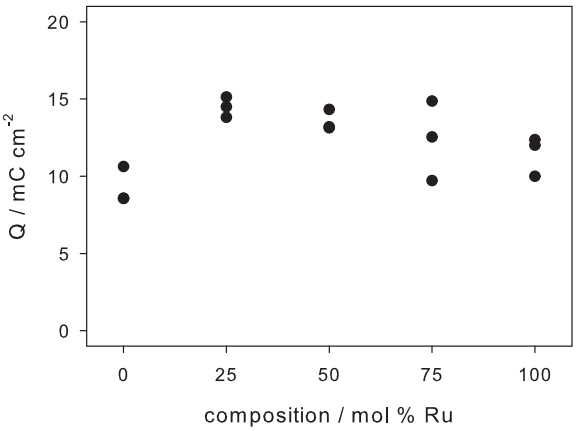

Figure 5: Outer charge (Q) of 20 wt% $Ir_xRu_{1-x}O_2$ on ATO nanoparticles as a function of Ru content in 0.5 mol L^{-1} H_2SO_4.

The effect of $Ir_{0.5}Ru_{0.5}O_2$ loading on the ATO nanoparticles has also been examined with the results indicating that decreasing the loading reduces the charge from the $Ir_{0.5}Ru_{0.5}O_2$ (Fig. 6). When these results are normalised by loading, we find that the dispersion of the IrO_2-RuO_2 is increases with decreasing loading, indicating that as the loading decreases so does cluster size.

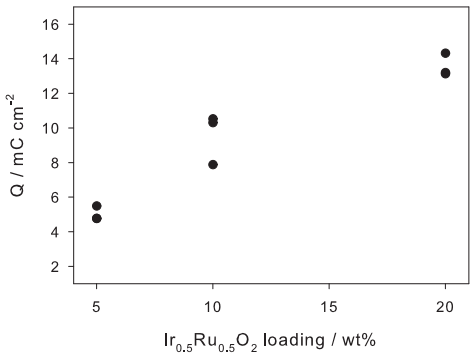

Figure 6: Outer charge (Q) as a function of $Ir_{0.5}Ru_{0.5}O_2$ loading on ATO in 0.5 mol L^{-1} H_2SO_4.

The performance of the prepared electrocatalysts towards oxygen evolution was examined by performing slow potential scans from 1 to 1.45 V at 0.5 mV s^{-1} in 0.5 mol L^{-1} H_2SO_4 (Fig. 7). Linear Tafel regions are observed over a limited current density range due to gas evolution beginning to influence the curve after around 1 mA cm^{-2}. Here we report the potential at 1 mA cm^{-2} as a measure of the electrocatalytic performance. The ruthenium content of the catalyst has a clear effect on the electrocatalytic performance (Fig. 8 A), with the overpotential decreasing with ruthenium content. This is in line with DSA literature which clearly shows that RuO_2 is more active

for oxygen evolution than IrO_2.

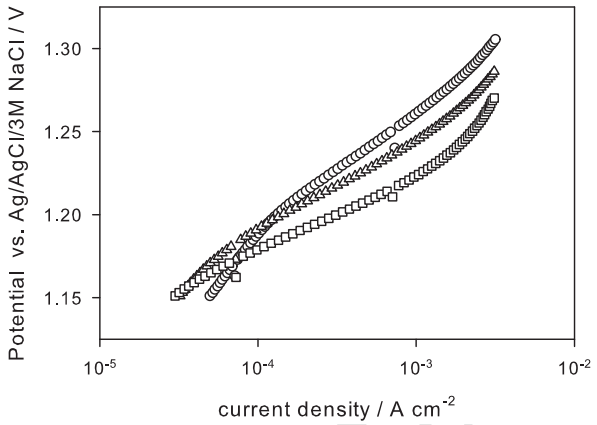

Figure 7: Polarisation curves of 20% $Ir_xRu_{1-x}O_2$ on ATO nanoparticles in 0.5 mol L^{-1} H_2SO_4. ($\circ$ = $Ir_{0.75}Ru_{0.25}O_2$, $\triangle$= $Ir_{0.50}Ru_{0.50}O_2$, $\square$= RuO_2). The curves have have been IR corrected using the solution resistance determined by electrochemical impedance spectroscopy at 1.2 V

Decreasing the loading below 20 wt% results in a decrease in the performance of these electrocatalysts towards oxygen evolution (Fig. 8 B). As we will show below, this reduction in performance is due to both a decrease in the electrochemically active surface area and specific electrocatalytic activity. We suggest that for practical electrolysers, it is probably better to use electrocatalysts with higher loadings so that higher current densities can be maintained at similar potentials, although to make conclusive recommendations one must also consider the stability and cost of each electrocatalyst which is beyond the present investigation.

Comparing the results with the performance of other IrO_2-RuO_2 based

nanoparticles and IrO_2-RuO_2 based DSA layers reveals that by coating ATO with IrO_2-RuO_2 clusters, a similar or better low current density performance can be obtained with considerably less of the expensive noble metal components thus decreasing the cost of the electrode material (Table 1). We believe this is almost soley due to the very high dispersion of the noble metal oxides facilated by the preparation procedure used in this work.

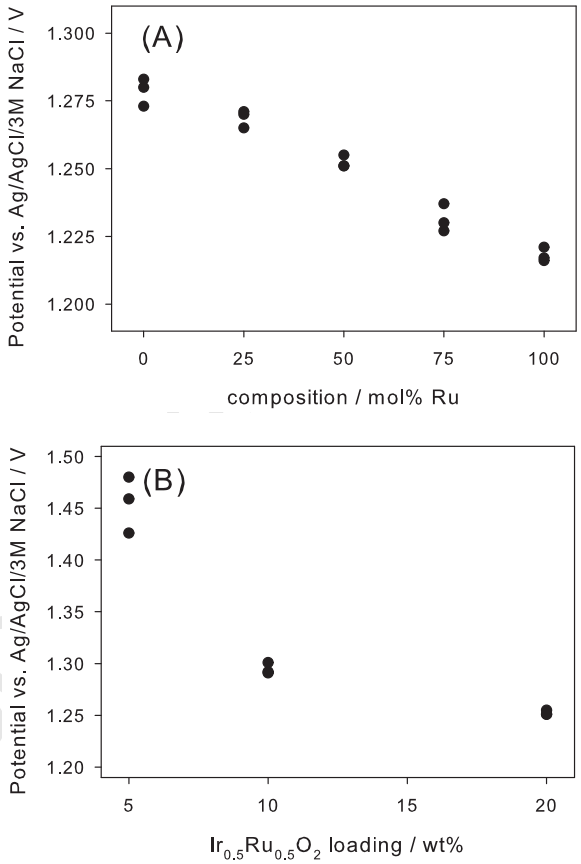

Figure 8: Potential of $Ir_xRu_{1-x}O_2$ on ATO nanoparticles at 1 mA cm^{-2} as a function of (A) coating composition and (B) $Ir_{0.5}Ru_{0.5}O_2$ loading in 0.5 mol L^{-1} H_2SO_4.

Table 1: Comparison of oxygen evolution performance in 0.5 mol L^{-1} H_2SO_4.

IrO_2-RuO_2 loading (mg cm^{-2})	E at 1 mA cm^{-2} (V)	Catalyst type	Reference
0.16	1.279	20 wt% IrO_2 on ATO	this work
0.16	1.252	20 wt% $Ir_{0.5}Ru_{0.5}O_2$ on ATO	this work
0.16	1.218	20 wt% RuO_2 on ATO	this work
0.78	1.291	$Ir_{0.7}Sn_{0.3}O_2$ particles	[4]
0.70	1.279	$Ir_{0.7}Ta_{0.3}O_2$ particles	[42]
1.00	1.266	IrO_2 particles	[42]
1.00	1.254	$Ir_{0.6}Ru_{0.4}O_2$ particles	[42]
5.00	1.296	IrO_2 DSA layer	[43]
1	1.231	$Ir_{0.5}Ru_{0.5}O_2$ DSA layer	[41]

To further understand how supporting the $Ir_xRu_{1-x}O_2$ phase on ATO nanoparticles influences the performance of the electrocatalyst towards the oxygen evolution reaction, we have calculated the specific electrocatalytic activity. This was determined by normalising the current density with the electrochemically active surface area (Q_{outer}) as found by cyclic voltammetry. The potential at 0.02 A C^{-1} is used to compare the specific electrocatalytic activity as this normalised current density lies within the linear regions of the polarisation curves for all samples. We have assumed that the charge per active Ru or Ir site is independent of oxide composition (i.e. 2 electrons per active Ir or Ru site). At very low loadings this assumption may not be valid as the support may alter the solid-state redox transitions on the Ir or Ru surface species. This possibility is part of our ongoing investigations. Here we find that the specific electrocatalytic activity increases with both increasing Ru content and loading (Fig. 9). The increase in activity with Ru content is simply explained by the higher activity of RuO_2 compared to IrO_2, a fact which is well established in DSA literature.

The decrease in specific activity with decreasing loading is more complex and requires analysis of the reaction mechanism. This is best done by considering the Tafel slope, which we found to increase from around 60 to 90 mV as the $Ir_{0.5}Ru_{0.5}O_2$ loading decreased from 20 to 5 wt% (Fig. 10 A). This trend is opposite from that described elsewhere which showed that as RuO_2 pseudocapacitive charge decreases the Tafel slope increases towards the value for single crystals [45]. Because the proposed mechanisms for the oxygen evolution reaction require adjacent reaction sites for desorption and recombination steps, we suggest that the very small clusters $Ir_xRu_{1-x}O_2$ (which occur on the

5 wt% samples) do not have sufficient density of adjacent reaction sites for the catalyst to faciliate rapid intermediate rearrangement and desorption. With the resulting high coverage of hydroxyl groups, the water discharge step begins to limit the reaction rate and the Tafel slope increases. Thus we suggest there must be an optimum in the cluster size at which the density of adjacent reaction sites permits rapid rearrangement and desorption of reaction intermediates. Others have related the electrocatalytic activity of $Ir_xTi_{1-x}O_2$ DSA electrodes to the availability of adjacent Ir–Ir pairs [46] and explained the loss of activity of Pt nanoparticles towards the oxygen reduction reaction using arguments based on the density of appropriate reaction sites [47]. Interestingly, Ferro and De Battisti [17] showed that for clusters of RuO_2 supported on boron-doped diamond, the Tafel slope of the chlorine evolution reaction decreased with decreasing RuO_2 cluster size. This change in the reactions rate determining step was suggested to be a result of a beneficial spill-over mechanism. In this work, any spill-over of reaction intermediates from the $Ir_xRu_{1-x}O_2$ clusters to the ATO support does not promote the oxygen evolution reaction.

As the XPS analysis suggested changes to the Ir electronic structure as the Ru content in the $Ir_xRu_{1-x}O_2$ coating varied, we also analysed the Tafel slope as a function of the $Ir_xRu_{1-x}O_2$ composition (Fig. 10 B). Here we find that the rate determining step of the reaction mechanism is influenced by composition in a similar fashion to elsewhere [41, 45, 48] with a Tafel slope of around 60 mV dec^{-1} for high iridium contents and 40 mV dec^{-1} for high ruthenium contents.

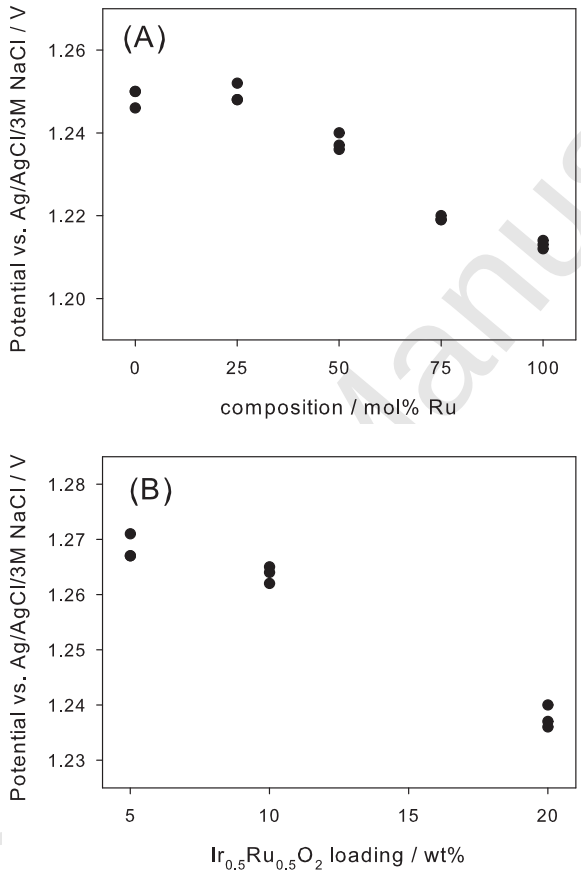

Figure 9: Specific electrocatalytic activity (Potential at a Q_{outer} normalised current density of 0.02 A C^{-1}) as a function of (A) composition of $Ir_xRu_{1-x}O_2$ on ATO nanoparticles and (B) $Ir_{0.5}Ru_{0.5}O_2$ loading in 0.5 mol L^{-1} H_2SO_4. Lower potentials indicate increased specific electrocatalytic activity

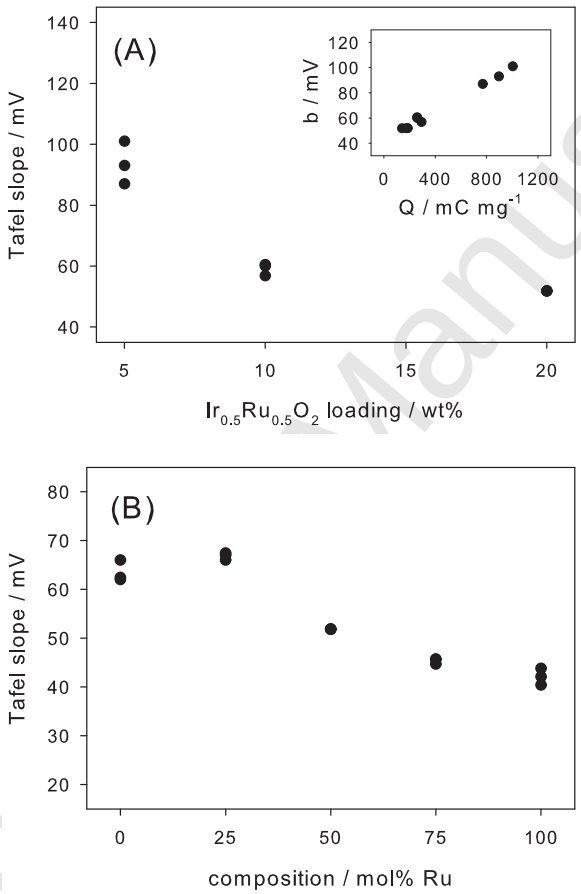

Figure 10: (A) Tafel slope as a function of $Ir_{0.5}Ru_{0.5}O_2$ loading and (B) composition of $Ir_xRu_{1-x}O_2$ on ATO nanoparticles in 0.5 mol L^{-1} H_2SO_4. Insert in (A) shows the Tafel slope as a function of pseudo-capacitive charge.

4. Conclusions

Thermal decomposition of $IrCl_3$ and $RuCl_3$ on ATO nanoparticles result in XRD amorphous clusters on the surface of the ATO. XPS analysis reveals that the clusters are likely to be $Ir_xRu_{1-x}O_2$ and that there is an interaction between the $Ir_xRu_{1-x}O_2$ and the ATO. Comparing the shape of cyclic voltammograms with DSA literature confirms that the supported electrocatalysts behave as $Ir_xRu_{1-x}O_2$. Analysis of the pseudo–capacitive charge shows that the electrochemically active surface is dependent of the $Ir_xRu_{1-x}O_2$ composition, although much less so than DSA type layers, most likely due to the high dispersion of the $Ir_xRu_{1-x}O_2$ phase on the surface of the ATO. Decreasing the loading results in a significant decrease in the total available electrochemically active surface area. This investigation also reveals that if active $Ir_xRu_{1-x}O_2$ clusters are too small, the specific electrocatalytic activity decreases due to insufficient density of adjacent active sites required for the oxygen evolution reaction. At a $Ir_xRu_{1-x}O_2$ loading of 20 wt%, the prepared electrocatalysts have similar performance than many literature reports, despite the low quantity of noble metals, suggesting that these oxides maybe useful anodes for PEM water electrolysers.

Acknowledgements

The authors would like to acknowledge the financial support from the Foundation of Research, Science and Technology (MAUX0602), and travel funding from the New Zealand Synchrotron Group for the diffraction analysis. This research was undertaken on the Powder Diffraction beamline at the Australian Synchrotron, Victoria, Australia (experiment PD665). The views

expressed herein are those of the authors and are not necessarily those of the owner or operator of the Australian Synchrotron.

References

[1] R. Hutchings, K. Müller, S. Stucki, J. Mater. Sci. 19 (1984) 3987.

[2] A. Marshall, S. Sunde, M. Tsypkin, R. Tunold, Int. J. Hydrogen Energy 32 (2007) 2320.

[3] A. Marshall, B. Børresen, G. Hagen, S. Sunde, M. Tsypkin, R. Tunold, Russ. J. Electrochem. 42 (2006) 1134.

[4] A. Marshall, B. Børresen, G. Hagen, M. Tsypkin, R. Tunold, Electrochimica Acta 51 (2006) 3161.

[5] E. Rasten, G. Hagen, R. Tunold, Electrochim. Acta 48 (2003) 3945.

[6] E. Slavcheva, I. Radev, S. Bliznakov, G. Topalov, P. Andreev, E. Budevsk, Electrochim. Acta 52 (2007) 3889.

[7] S. Song, H. Zhang, X. Ma, Z. Shao, R. Baker, B. Yi, Int. J. Hydrogen Energy 33 (2008) 4955.

[8] A. Tsueng, S. Dhara, Electrochim. Acta 20 (1975) 681.

[9] S. Hall, S. Subramanian, G. Teeter, B. Rambabu, Solid State Ionics 175 (2004) 809.

[10] V. Hughes, B. McNicol, J. Chem. Soc. Faraday Trans. 75 (1979) 2165.

[11] K. Lee, I. Park, Y. Cho, D. Jung, N. Jung, H. Park, Y. Sung, J. Catalysis 258 (2008) 143.

[12] Z. Galus, in: A. Bard, R. Parsons, J. Jordan (Eds.), Standard Potentials in Aqueous Solution, Marcel Dekker, 1985, p. 189.

[13] B. Merzougui, S. Swathirajan, J. Electrochem. Soc. 153 (2006) A2220.

[14] N. Spătaru, X. Zhang, T. Spătaru, D. Tryk, A. Fujishima, J. Electrochem. Soc. 155 (2008) B264.

[15] O. Haas, S. Briskeby, O. Kongstein, M. Tsypkin, R. Tunold, B. Børresen, J. New Mater. Electrochem. Sys. 11 (2008) 9.

[16] G. Siné, I. Duo, B. El Roustom, G. Fóti, Ch. Comninellis J. Appl. Electrochem. 36 (2006) 847.

[17] S. Ferro, A. De Battisti J. Phys. Chem. B 106 (2002) 2249.

[18] E. Slavcheva, V. Nikolova, T. Petkova, E. Lefterova, I. Dragieva, T. Vitanov, E. Budevski, Electrochim. Acta 50 (2005) 5444.

[19] L. Ma, S. Sui, Y Zhai, J. Power Sources 177 (2008) 470.

[20] G. Lodi, A. D. Battisti, G. Bordin, C. D. Asmundis, A. Benedetti, J. Electroanal. Chem. 277 (1990) 139.

[21] C. Wagner, L. Davis, M. Zeller, J. Taylor, R. Raymond, L. Gale, Surf. Interface Anal. 3 (1981) 211.

[22] P. He, Anal. Chem 67 (1995) 986.

[23] B. Gržeta, E. Tkalčec, C. Goebbert, M. Takeda, M. Takahashi, K. Normura, M. Jakšić, J. Phys. Chem. Solids 63 (2002) 765.

[24] J. Moulder, W. Stickle, P. Sobol, K. Bomben, Handbook of x-ray photoelectron spectroscopy, Perkin-Elmer Corp, 1992.

[25] W. Dmowski, T. Egami, K. Swider-Lyons, C. Love, D. Rolison, J. Spectrosc. Relat. Phenom. 128 (2003) 59.

[26] L. Atanasoska, R. Atanasoska, S. Trasatti, Vacuum 40 (1990) 91.

[27] J. Augustynski, M. Koudelka, J. Sanchez, B. Conway, J. Electroanal. Chem. 160 (1984) 233.

[28] Y. Roginskaya, O. Morozova, E. Loubnin, A. Popov, Y. Ulitina, V. Zhurov, S. Ivanov, S. Trasatti, J. Chem. Soc., Faraday Transactions 89 (1993) 1707.

[29] G. Wertheim, H. Guggenheim, Phys. Rev. B 22 (1980) 4680.

[30] S. Hackwood, A. Dayem, G. Beni, Phys. Rev. B 26 (1982) 471.

[31] W. Morgan, W. Stec, J. Van Wazer, Inorg. Chem. 12 (1973) 953.

[32] I. Barin, Thermochemical data of pure subtances, VCH, Weinheim, 1989.

[33] Y. Roginskaya, T. Varlamova, M. Goldshtein, T. Belova, B. Galyamov, R. Shifrina, V. Shepelin, V. Fateev, Mater. Chem. Phys. 30 (1991) 101.

[34] C. Angelinetta, L. Atanasoska, R. Atanasoski, S. Trasatti, J. Electroanal. Chem. 214 (1986) 535.

[35] L. Burke, D. Whelan, J. Electroanal. Chem. 162 (1984) 121.

[36] S. Levine, A. Smith, Faraday Discuss. Soc 52 (1971) 290.

[37] R. Savinell, R. Zeller, J. Adams, J. Electrochem. Soc. 137 (1990) 489.

[38] B. Aurian-Biajeni, A. Kimball, L. Robblee, G. Kahanda, C. Tomkiewicz, J. Electrochem. Soc. 134 (1987) 2637–2638.

[39] I. Kodintsev, S. Trasatti, M. Rubel, A. Wieckowski, N. Kaufher, Langmuir 8 (1992) 283.

[40] S. Ardizzone, G. Fregonara, S. Trasatti, Electrochim. Acta 35 (1990) 263.

[41] F. Mattos-Costa, P. de Lima-Neto, S. Machado, L. Avaca, Electrochim. Acta 44 (1998) 1515.

[42] A. Marshall, B. Børresen, G. Hagen, M. Tsypkin, R. Tunold, Energy 32 (2007) 431.

[43] C. De Pauli, S. Trasatti, J. Electroanal. Chem. 538-539 (2002) 145.

[44] G. Chen, X. Chen, P. Yue, J. Phys. Chem. B 106 (2002) 4364.

[45] E. Guerrini, S. Trasatti, Russ. J. Electrochem. 42 (2006) 1017.

[46] K. Endo, Y. Katayama, T. Miura, T. Kishi, J. Appl. Electrochem. 32 (2002) 173.

[47] K. Kinoshita, J. Electrochem. Soc. 137 (1990) 845.

[48] R. Kötz, S. Stucki, Electrochim. Acta 31 (1986) 1311.